Probing coherent phonons in the advanced undergraduate laboratory **⊘**

Nicholas J. Brennan; Joseph Peidle; Anna Wang-Holtzen; Jieping Fang; Kathryn Ledbetter; Matteo Mitrano



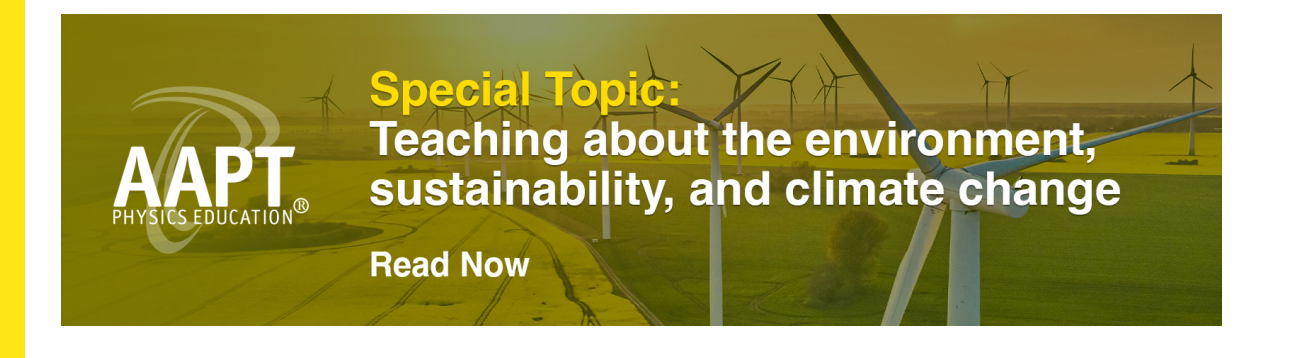
Check for updates

Am. J. Phys. 92, 693-702 (2024) https://doi.org/10.1119/5.0190019











INSTRUCTIONAL LABORATORIES AND DEMONSTRATIONS

John Essick, Editor

Department of Physics, Reed College, Portland, OR 97202

Articles in this section deal with new ideas and techniques for instructional laboratory experiments, for demonstrations, and for equipment that can be used in either. Although these facets of instruction also appear in regular articles, this section is for papers that primarily focus on equipment, materials, and how they are used in instruction. Manuscripts should be submitted using the web-based system that can be accessed via the American Journal of Physics home page, ajp.aapt.org, and will be forwarded to the IL&D editor for consideration.

Probing coherent phonons in the advanced undergraduate laboratory

Nicholas J. Brennan, a) Joseph Peidle, b) Anna Wang-Holtzen, c) Jieping Fang, d) Kathryn Ledbetter, e) and Matteo Mitrano (1)

Department of Physics, Harvard University, Cambridge, Massachusetts 02138

(Received 2 December 2023; accepted 30 May 2024)

Ultrafast optical spectroscopy is an effective experimental technique for accessing electronic and atomic motions in materials at their fundamental timescales and studying their responses to external perturbations. Despite the important insights that ultrafast techniques can provide on the microscopic physics of solids, undergraduate students' exposure to this area of research is still limited. In this article, we describe an ultrafast optical pump-probe spectroscopy experiment for the advanced undergraduate instructional laboratory, in which students can measure coherently excited vibrations of the crystal lattice and connect their observations to the microscopic properties of the investigated materials. We designed a simple table-top apparatus based on a commercial Er-fiber oscillator emitting 50-fs pulses at 1560 nm and at 100 MHz repetition rate. We split the output into two beams, using one of them as an intense "pump" to coherently excite phonons in selected crystals, and the other as a weaker, delayed "probe" to measure the transient reflectivity changes induced by the pump. We characterize the ultrafast laser pulses via intensity autocorrelation measurements and detect coherent phonon oscillations in the reflectivity of Bi, Sb, and 1*T*-TaS₂. We then discuss the oscillation amplitude, frequency, and damping in terms of microscopic properties of these systems. © 2024 Published under an exclusive license by American Association of Physics Teachers.

https://doi.org/10.1119/5.0190019

I. INTRODUCTION

In recent decades, ultrafast laser sources have transformed experimental condensed matter physics by enabling real-time observation of electronic and atomic dynamics.¹ Femtosecond laser pulses are able to capture quantum mechanical processes in solids at their fundamental timescales, which typically range from femtoseconds to nanoseconds.³ By leveraging differences in the time constants of electronic, magnetic, and structural dynamics, ultrafast optical spectroscopy is able to directly investigate the interactions among these subsystems and offer insights that complement those obtained from time-integrated spectroscopic methods.⁶ Furthermore, since photoexcitation often occurs faster than the characteristic relaxation times, this experimental technique is suited to probe phenomena occurring uniquely when materials are driven out of equilibrium.^{7,8} In a typical ultrafast optical spectroscopy experiment, the laser light is separated into two beams, one intense ("pump") to perturb a material, and a weaker one ("probe") for monitoring its pump-induced dynamics. The dynamical response of the photoexcited sample is measured in a stroboscopic fashion by varying the relative time delay

between the two pulses and acquiring data at a fixed repetition rate.

Despite being increasingly relevant to condensed matter physics, materials science, chemistry, as well as atomic, molecular, and optical (AMO) physics, ultrafast optical spectroscopy is currently underrepresented in the undergraduate curriculum. As a consequence, the training of future researchers in this area often starts only at the graduate level and without prior connections to fundamental undergraduate coursework. In the context of the undergraduate laboratory course, a major obstacle for the diffusion of ultrafast optical spectroscopy is the high technological cost. Ultrafast optical setups can be technically advanced and complex to maintain. In addition, femtosecond laser systems are generally expensive (with prices of order \$100 000 or more just for the laser source), and require highly specialized environments (e.g., stable in temperature and relative humidity) to ensure reliable operation. These factors have historically hindered the integration of ultrafast techniques in traditional educational laboratories. Earlier work to increase undergraduate exposure to time-resolved experiments mainly focused on ultrafast optical processes, 9,10 while the emphasis has only recently shifted toward the physical and chemical insights that they can provide. 11,12

Here, we demonstrate the construction and operation of an ultrafast pump-probe spectroscopy experiment for the advanced undergraduate laboratory. The experiment specifically focuses on the study of coherent phonon generation in solids, although the setup is versatile and can be adapted for other ultrafast studies. To eliminate the need for stable environmental conditions and to reduce costs, we designed a table-top pump-probe apparatus based on a commercial Er fiber oscillator emitting 50-fs pulses at 1560 nm and at 100 MHz repetition rate. Our experiment allows students to (a) characterize ultrafast laser pulses via second harmonic generation (SHG)-based intensity autocorrelation and (b) excite and measure coherently excited phonons in bismuth (Bi), antimony (Sb), and tantalum disulfide (1*T*-TaS₂). These materials all exhibit well-characterized coherent oscillations in the terahertz (THz) range and their responses can be studied as functions of incident fluence, i.e., the time-integrated flux per unit area of the pump beam, to investigate their microscopic origin. By analyzing experimental data at room temperature and for different excitation regimes, we interpret ultrafast reflectivity changes in terms of microscopic properties of the crystal lattice, thus demonstrating the value of ultrafast optical spectroscopy as a probe of materials' physics. Since the physics of coherent phonon generation seamlessly blends concepts from introductory curricula in wave phenomena and solid state through upper-level physics coursework (such as phonons and classical damped-driven oscillators), this experiment efficiently connects ultrafast spectroscopy with undergraduate-level physics and is ideally positioned to integrate this growing research area in the undergraduate curriculum. To successfully complete this experiment, undergraduates at the junior/senior level should be familiar with the physics of driven and damped harmonic oscillators, with notions of symmetry and lattice vibrations in crystals, as well as with basic data analysis techniques.

The article is structured as follows. In Sec. II, we introduce the physics of coherent phonon generation before presenting the experimental setup in Sec. III. In Sec. IV, we report the results of our time-resolved reflectivity measurements on Bi, Sb, and 1T-TaS2 and discuss how observed phonon amplitude, frequency, and damping depend on the microscopic properties of these systems. Section V presents our conclusions. Additional information regarding equipment cost is included in Appendix.

II. COHERENT PHONON GENERATION

One of the first applications of ultrafast optical spectroscopy has been the study of coherent phonon generation in solids. 13–15 Phonons are quantized vibrations of the lattice, whose symmetry and dispersion strictly depend on the crystallographic properties of a material. 16,17 In the longwavelength limit, phonons are either acoustic or optical. The former involve a collective motion of the ionic basis in the unit cell and are responsible (among other things) for the transmission of sound, while the latter are characterized by ionic motions within the basis, which typically have higher energies. Phonons that change the dipole moment of the unit cell during their vibration are defined as infrared (IR)-active. Those that alter the lattice polarizability are known as Raman-active. If the crystal has inversion symmetry, phonons are exclusively IR- or Raman-active and their ionic displacements will be odd or even under inversion.

At equilibrium, phonons are excited due to the sample temperature and are generally incoherent, meaning that their oscillations are not locked in a constant phase relation. However, a sudden laser excitation with pulses shorter than the oscillation period can excite these lattice vibrations in a coherent fashion and induce well-defined oscillations of the physical properties of a material. 18,19 Depending on whether a material is transparent or opaque, the generation of coherent phonons manifests in different ways. In transparent media, the pump is not absorbed and phonons are excited by setting the nuclei in motion around their equilibrium positions through a force proportional to the pump intensity. This mechanism is in essence a Raman process, commonly referred to as impulsive stimulated Raman scattering (ISRS). 18,20 In opaque materials, this process coexists with a distinct excitation mechanism, namely the displacive excitation of coherent phonons (DECP).²¹ In DECP, the absorbed pump leads to a nonequilibrium electron distribution. Thanks to the electron-phonon interaction, the phonons can couple to these real charge density fluctuations persisting over a few periods and lead to an instantaneous shift of the equilibrium ion positions, followed by oscillations around the new displaced position.

In this experiment, we focus on the physics of the DECP mechanism in Bi, Sb, and 1T-TaS₂ crystals. 14,15,18-20,22 In these materials, the pump photon absorption induces electronic transitions into higher-energy states [see Fig. 1(a)]. Since electrons are much lighter than the lattice ions, these transitions occur over much shorter timescales than those of the nuclear motions and will quickly lead to a new electronic distribution. The sudden change of the electronic environment spatially displaces the ions by an amount ΔQ along the direction of the phonon eigenvectors that maintain the symmetry of the unit cell. The nuclei then begin to coherently oscillate. These coherent phonons are typically Ramanactive and of A_{1g} symmetry. The Mulliken symbol A_{1g} indicates that the mode is symmetric with respect to rotation about the principal axis of the crystal (A), as well as to all the symmetry operations of the point group ("1" subscript), and to inversion through the center of the unit cell ("g" subscript).²³ As an example, we show in Fig. 1(b) the displacements of the Bi A_{1g} phonon.

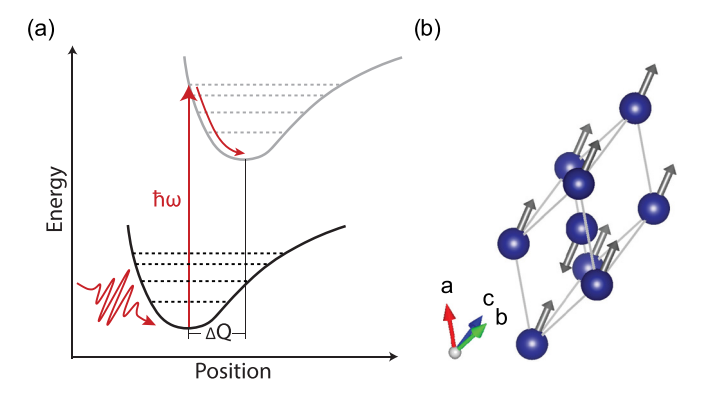


Fig. 1. (a) Sketch of the displacive excitation of coherent phonons. A laser pulse (red) is absorbed by the sample and excites electrons from the ground state (black) into higher energy levels (gray). This charge redistribution induces a long-lived shift ΔO of the phonon coordinates and initiates a coherent oscillation of the nuclei around their new equilibrium position. Dashed lines represent the vibrational energy levels of the system. (b) Bismuth unit cell with displacements associated with a Raman-active A_{1,0} phonon mode shown as dark gray arrows.

694

For simplicity, in the following, we limit ourselves to the case that just one specific phonon is excited by the ultrafast pump laser. At a phenomenological level, the lattice nuclei oscillate according to the equation of motion of a driven damped harmonic oscillator, ^{15,19,24}

$$\mu^* \left(\frac{\partial^2 Q(t)}{\partial t^2} + 2\gamma_{ph} \frac{\partial Q(t)}{\partial t} + \omega_{ph}^2 Q(t) \right) = F^Q(t), \tag{1}$$

where μ^* is the reduced atomic mass, Q(t) is the phonon coordinate, ω_{ph} is the phonon angular frequency, γ_{ph} is the phonon damping coefficient, and F^Q is the driving force acting on the phonon coordinate Q as a function of time t. For the DECP, we define $F^{\mathcal{Q}}(t)/\mu^* = \kappa \rho(t)$, where κ is a proportionality constant, and $\rho(t)$ is the time-dependent electronic density. This expression accounts for the pump-induced electronic density change and assumes a linear ionic displacement. Since the electron dynamics are much faster than that of the ions, the electronic density change is sudden, and $F^{Q}(t)/\mu^{*}$ becomes $F^{Q}(t)/\mu^{*} = \kappa \Delta \rho \Theta(t)$, where $\Delta \rho$ is the charge density variation, and $\Theta(t)$ is a Heaviside step function. For a more general treatment of the electronic response, see Ref. 15. If one postulates that the nuclei do not immediately depart from their average equilibrium positions (Q(t=0)=0) and that the pump does not affect their average velocity [Q'(t=0)=0], ²⁴ the solution of the equation of motion for t > 0 reads

$$Q(t) = \frac{-\kappa \Delta \rho}{\mu^* \Omega \omega_{ph}^2} \left\{ \gamma e^{-\gamma t} \sin(\Omega t) + \Omega \left[e^{-\gamma t} \cos(\Omega t) - 1 \right] \right\}, \tag{2}$$

where $\Omega = \sqrt{\omega_{ph}^2 - \gamma_{ph}^2}$ is the usual damped oscillator frequency. In the limit of underdamped phonons $(\gamma^2 \ll \omega_{ph}^2)$, the $\sin(\Omega t)$ term becomes negligible and the coordinate displacement further simplifies to

$$Q(t) = -\frac{\kappa \Delta \rho}{\mu^* \omega_{ph}^2} e^{-\gamma t} \cos(\Omega t) + \frac{\kappa \Delta \rho}{\mu^* \omega_{ph}^2}.$$
 (3)

Hence, the phonons start to oscillate with a cosine behavior, a key feature of the DECP mechanism, and around a new equilibrium position given by the time-independent term of Eq. (3).

These oscillations produce a macroscopic modulation of the electronic properties of a material and can be directly probed by monitoring the time-dependent reflectivity R(t). At normal incidence and in air, the reflectivity is expressed as

$$R = \left| \frac{1 - \tilde{n}}{1 + \tilde{n}} \right|^2 = \frac{(1 - n_1)^2 + n_2^2}{(1 + n_1)^2 + n_2^2},\tag{4}$$

where $n_{1,2}$ are the real and imaginary parts of the complex refractive index $\tilde{n} = n_1 + in_2$. In a pump-probe experiment where the electronic density $\rho(t)$ and the phonon coordinates Q(t) are both perturbed by the pump laser, we can calculate the differential reflectivity change $\Delta R(t) = R(t) - R(t < 0)$ by expanding the reflectivity in both variables,

$$\frac{\Delta R(t)}{R} = \frac{1}{R} \left[\left(\frac{\partial R}{\partial \rho} \right) \rho(t) + \left(\frac{\partial R}{\partial O} \right) Q(t) \right]. \tag{5}$$

The first term will contribute an exponential due to the relaxation of the nonequilibrium electron redistribution, while the second term will encode the time-dependent coherent phonon oscillations. The phonon frequency is determined by the elastic constants of the crystal and the atomic masses involved in the oscillation, according to the well-known relationship $\omega_{\rm ph} = \sqrt{k/\mu^*}$ (with k being an elastic constant). The phonon damping quantifies instead the dephasing time of the coherent mode $\gamma = 1/T_2$.

Finally, the amplitude of the coherent phonon oscillation can be directly used to estimate the pump-induced ionic displacements U_0 of the lattice with sub-Å accuracy. The normalized reflectivity change due to the phonon displacement in Eq. (5) can also be expressed as

$$\frac{\Delta R(t)}{R} \sim D \frac{\partial \omega}{\partial Q} \hbar Q(t), \tag{6}$$

where

$$D = \frac{1}{R(\hbar\omega)} \frac{\partial R}{\partial \epsilon} (\hbar\omega) \frac{\partial \epsilon}{\partial \hbar\omega} (\hbar\omega),$$

with ϵ being the dielectric constant. The phonon amplitude depends instead on the incoming electric field $E(\omega)$ and Raman tensor $\Re_{Q}(\omega)$ as

$$Q \sim \frac{E(\omega)E^*(\omega)\Re_Q(\omega)}{\Omega_0\eta^2(\omega)\tau_l},\tag{7}$$

with $\eta(\omega) \equiv 1 + n_1(\omega) + in_2(\omega)$, Ω_0 is the pump frequency, and τ_l is the pump pulse duration. By combining these relations for an opaque medium and considering that the ionic displacement U_0 depends on the phonon coordinate Q through $U_0(\Omega) = (1/\sqrt{\rho})(Qe^{i\Omega t} + Q^*e^{-i\Omega t})$ (with ρ being the sample density), one can calculate the ionic displacements with the compact relation (see Appendix A of Ref. 25),

$$U_0^2 \sim \frac{\Delta R}{R} \frac{|E(\omega)|^2 (2i\epsilon_2/\hbar\omega)^2}{\epsilon \rho \Omega \tau_i D},\tag{8}$$

with ϵ_2 and ϵ indicating imaginary part and modulus of the sample dielectric constant, respectively.

III. IMPLEMENTATION

A. Ultrafast laser source

We select an Er fiber laser (ELMO-ELMA by Menlo Systems) over a Ti:sapphire source. 10,12 The ELMO fiber oscillator generates 1560 nm, horizontally polarized light at a repetition rate of 100 MHz and with a pulse duration of 50 fs, which is then amplified by the ELMA unit to reach 180 mW average power. The fiber laser has a small volume $(275 \times 75 \times 110 \,\mathrm{mm}^3)$ including the baseplate) and does not require a specialized laboratory environment, as it reliably operates at temperatures between 15 and 35 °C. These features make this system particularly apt for the realization of compact table-top spectroscopy experiments in a more traditional laboratory space. Furthermore, the laser itself does not require hands-on alignment, thereby reducing the entry barrier for students and shifting the focus to the spectroscopic goals of the experiment. While we opted for a commercial laser costing approximately \$32000 (i.e., about a factor of two lower than a typical Ti:sapphire oscillator) to facilitate rapid

deployment, mode-locked fiber lasers of comparable specifications have been demonstrated at costs as low as \$7400.²⁶

B. Pump-probe spectroscopy setup

The apparatus used for this ultrafast optical spectroscopy experiment is shown in Fig. 2. After emerging from the laser via an optical fiber, the ultrafast pulses are fed into the free-space spectroscopy setup through a fiber coupler. The beam is then split into pump and probe beams by a 90:10 (R:T) beamsplitter. The pump light is focused and mechanically chopped at 2–10 kHz before being recollimated by a second lens. The chopped beam is then directed to a motorized delay stage with a mounted retroreflector to vary the relative pump-probe delay. To control the incident power at the sample, the pump passes through a $\lambda/2$ waveplate in series with a horizontally aligned linear polarizer before being focused onto the sample surface. The spot size is typically less than 30 μ m.

The probe light is directed onto a retroreflector on a separate, manual delay stage, which is used to accommodate bigger changes of the optical paths before performing pumpprobe experiments. The horizontally polarized light is then rotated to vertical polarization by using another set of $\lambda/2$ waveplate and linear polarizer before being focused onto the sample surface with a beam waist of $30 \,\mu\mathrm{m}$ (i.e., similar to pump). The pump and probe beams are then spatially overlapped by measuring the transmission through a 50-µmdiameter pinhole with a power meter. The spatial overlap is crucial for measuring dynamics exclusively from the photoexcited region of the sample, thereby enhancing the visibility of the pump-induced signal. The two beams are then temporally overlapped by first ensuring that pump and probe path lengths from the beamsplitter to the sample surface are roughly equal (within ~ 1 cm). We then proceed with a finetuning of the temporal delay by moving the motorized stage and looking for the autocorrelation signal of the two beams in a 100- μ m-thick type-I β -barium borate (BBO) crystal (see procedure described in Sec. IV A). Using a camera to visualize the second harmonic beams downstream of the BBO, we scan the position of the pump delay stage until a third spot

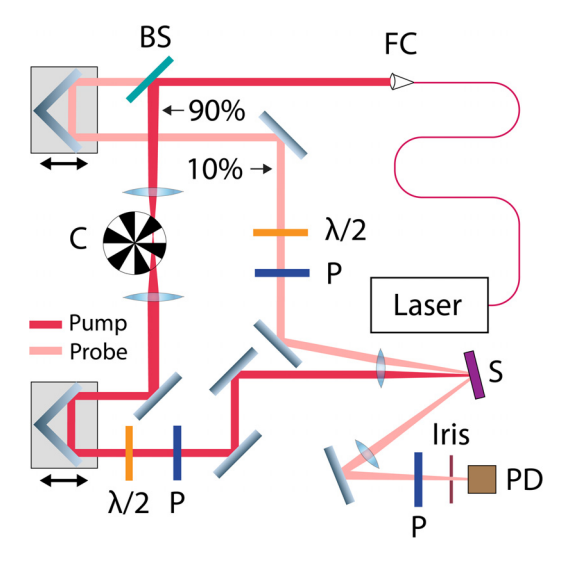


Fig. 2. Schematic of ultrafast optical setup (see the text for description). Optical components include: beamsplitter (BS), polarizer (P), fiber coupler (FC), beam chopper (C), half waveplate ($\lambda/2$), photodiode (PD), sample (S), and an Er fiber laser (laser). Retroreflectors on delay stages (gray rectangles) are depicted at right angle geometries on each delay stage.

appears in the middle. Once the third beam is identified, we optimize the power of the new beam using a photodiode and lock-in amplifier to locate time zero and characterize the pulse duration through an intensity autocorrelation measurement. At this point, we replace the BBO with a sample and complete the setup by assembling the detector arm.

In this experiment, we focus on opaque materials and measure pump-induced changes of the sample reflectivity. Hence, we block the pump light reflected by the sample and collect the probe beam with a steering mirror and a lens focusing the light onto a large area Ge-based photodiode (455 ns rise time). Since pump and probe are degenerate at 1560 nm, particular care must be exercised in preventing any pump light from reaching the detector and creating an interference signal in the data. For this purpose, in addition to having orthogonalized the polarizations of the two beams, we place an additional vertically oriented polarizer in the detector arm and a narrow iris in front of the detector. We also add shielding around the photodiode to further suppress stray pump light. The photodiode is connected to an SRS830 lock-in amplifier with a $50-\Omega$ termination to achieve its specified response time. The lock-in amplifier is referenced to the output signal of the mechanical chopper. The lock-in amplifier measures the difference in reflectivity (ΔR) between the "pump on" and "pump off" conditions. In order to measure the total reflectivity for normalization, one then chops the probe while blocking the pump immediately before or after the pump-probe scan.

The data acquisition is performed through a custom LabVIEW-based graphical interface that controls the motorized stage and measures the analog output from the lock-in. The software allows students to automatically run scans and collect and save data from the lock-in amplifier. The same software is used to both measure the ultrafast laser pulse duration and the pump-probe signal coming from the samples.

We note that the setup is designed to be modular and adaptable, particularly at the overlap region where a subsetup replaces the sample with a BBO crystal for SHG intensity autocorrelation measurements. The sample stage and detector arm are left unassembled for students to construct. This assembly contributed to developing the students' sense of ownership of the apparatus without the difficulty of aligning the entire pump-probe setup.

C. Laser safety

The ELMO-ELMA system is a Class 3B laser, meaning that its permitting and deployment in undergraduate laboratories is more straightforward than typical Class 4 lasers. However, students are required to take appropriate laser safety training and wear protective glasses at all times. In our experiment, we choose F42.P1M01.5000 safety glasses by Laservision, which ensure OD4+ and OD2+ attenuation at 1560 and 780 nm, respectively. Furthermore, we recommend laterally enclosing the entire optical setup with blackout material (e.g., Thorlabs 4.76-mm-thick black construction hardboard) to avoid stray light exiting the setup.

IV. RESULTS

The experiment implemented in our advanced laboratory curriculum requires the students to: (1) characterize the ultrafast pulse duration by using SHG intensity autocorrelation, (2) measure coherent phonon oscillations in the transient reflectivity of Bi, Sb, and 1T-TaS $_2$ crystals, and (3) study

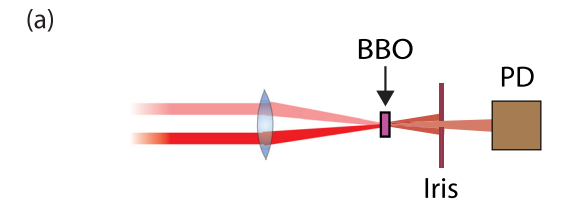
their behavior as a function of the incident pump fluence (energy per unit area). In the following, we show representative data for each of these experiments.

A. Ultrafast pulse duration measurement

Ultrafast optical spectroscopy experiments require accurate knowledge of the laser pulse properties. Although the spectrum of an ultrafast pulse can be measured using standard methods like grating spectrometers, its duration is usually too short for regular photodetectors and oscilloscopes. This approach requires special pulse-duration measurement techniques. One possible experimental strategy is to use the pulse itself as a probe in an autocorrelation measurement. We consider an ultrafast pulse with an electric field $a(t) = |a(t)|e^{i\phi(t)},$ where |a(t)| is the field amplitude, and $\phi(t)$ is the temporal phase. A field autocorrelation measurement in a Michelson interferometer yields a function $G_1(\tau) \sim |\langle a(t)a^*(t-\tau)\rangle|/\langle |a(t)|^2\rangle$, which linearly correlates the electric field amplitude of the sampled beam. $G_1(\tau)$, however, only allows for quantifying the coherence time of the electric field, or equivalently, the minimum expected pulse duration $\Delta \tau$ based on the inverse optical bandwidth $(\Delta \tau \sim 1/\Delta \nu)$, where $\Delta \nu$ is the spectral bandwidth of the laser pulse).²⁷ The coherence time is not necessarily coincident with the pulse duration and is defined as the decay time of the field correlation function. Being solely determined by the spectral content, the coherence time makes it impossible to differentiate between two ultrafast pulses having identical spectral bandwidths, but different durations.

A more effective approach is to perform an intensity autocorrelation measurement by inserting a nonlinear element in the Michelson interferometer.^{27,28} Here, we exploit secondharmonic generation (SHG), a nonlinear optical process in which a crystal generates light at twice the input optical frequency ω_0 . We recombine the pump and probe beams (with frequency ω_0) on a BBO crystal to generate sumfrequency light at $2\omega_0$ and measure its intensity as a function of the relative delay τ between the two pulses. Since the crystal response is nonlinear, the SHG signal is more intense when the two incident pulses overlap in time. In a noncollinear geometry, i.e., if the two beams are overlapped on the BBO with a nonzero relative angle, the transverse momentum of the input beams cancel in the correlated beam and the sum-frequency signal becomes background-free. The SHG signal is proportional to $\langle P_{\rm SHG} \rangle \sim G_2(\tau)$, where $G_2(\tau) = \langle I(t)I(t-\tau)\rangle/\langle |I(t)|^2\rangle$ is the normalized intensity autocorrelation function and $I(t) \sim |a(t)|^2$. The SHG power will peak at the overlap between the two pulses and then smoothly decay to zero when the two pulses are delayed by a time interval larger than the pulse duration. The pulse duration can therefore be estimated from the FWHM of the correlation trace (which we call $\Delta \tau$). The intensity full width at half maximum (FWHM) Δt of the pulse is finally determined by dividing the intensity autocorrelation FWHM $\Delta \tau$ by a pulse-shape-specific deconvolution factor. For a Gaussian pulse, the deconvolution factor is $\sqrt{2}$, and $\Delta t = \Delta \tau / \sqrt{2}$. We note that a non-collinear SHG autocorrelation measurement only yields the duration of the pulse envelope and does not provide information about the temporal phase of the field.

In our setup, we replace the sample with the BBO configuration depicted in Fig. 3(a) by positioning the crystal at the pump-probe overlap and tuning the BBO angles to maximize the SHG signal from each of the beams. We then measure



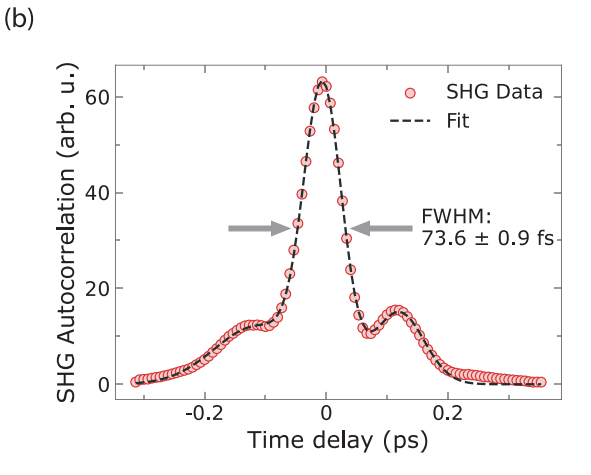


Fig. 3. (a) Detail of the SHG autocorrelation setup. Intensity autocorrelation measurements are performed by replacing the sample in Fig. 2 with a BBO crystal and by detecting the sum-frequency signal in transmission with a photodiode (PD) after rejecting the other SHG beams with an iris. (b) SHG intensity autocorrelation data (open red symbols) with a three-Gaussian fit (black dashed line) accounting for main peak and side lobes.

the average power in between the two SHG spots by using a photodiode while scanning the relative delay. A typical SHG autocorrelation measurement is shown in Fig. 3(b). In our setup, we observe two lobes adjoining the main autocorrelation peak, which are due to the shape of the amplified spectrum in the frequency-domain after the nonlinear amplifier and the pulse compression in the fiber.²⁹ While the autocorrelation signal should always be symmetric around the zero time delay, our data show a slight intensity asymmetry in the side lobes. A frequent cause of small asymmetries in the autocorrelation trace is a minor misalignment of the moving autocorrelator mirror, which might alter the overlap condition on the BBO crystal. We phenomenologically fit the autocorrelation trace as a sum of three Gaussians, and the FWHM of the main peak is found to be 73.6 ± 0.9 fs, thus implying a pulse duration of 52.0±0.6 fs, consistent with the source specifications.

B. Coherent phonon dynamics

After quantifying the pulse duration, we proceed with the coherent phonon generation measurement. We revert the setup back to the reflection geometry shown in Fig. 2 and measure the reflected probe off of the sample while scanning the pump-probe delay through time zero. In Figs. 4(a)–4(e), we report representative differential reflectivity changes in Bi, Sb, and 1T-TaS₂. The interference signal from the reflected pump was suppressed by closing an iris in front of the detector and selecting smooth areas of the sample surfaces. All the ΔR measurements reported in this paper are performed at room temperature and normalized to the equilibrium reflectivity R as measured by chopping the probe and blocking the pump. After the pump arrival, the sample reflectivity suddenly decreases and relaxes back to equilibrium on picosecond

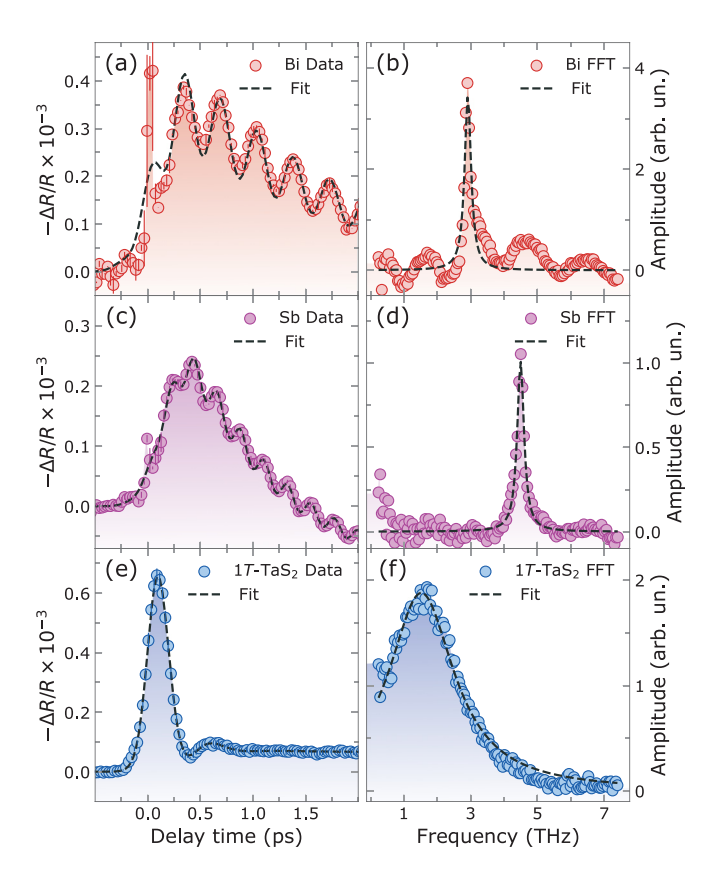


Fig. 4. Time-dependent differential reflectivity $\Delta R/R$ (absolute values) and Fourier transform amplitude of the coherent phonon oscillations for (a) and (b) Bi, (c) and (d) Sb, and (e) and (f) $1\,T\text{-}\mathrm{TaS}_2$. Experimental data are represented with circles, while dashed black lines indicate fits to the data. All curves are measured at room temperature and for an incident pump fluence of $65\pm 1\,\mu\,\mathrm{J/cm^2}$ for Bi, Sb, and $1\,T\text{-}\mathrm{TaS}_2$. Each dataset is an average of two 12-minutes scans with a 100-ms lock-in constant and a 500-ms settle time.

timescales. The time-dependent behavior consists of an electronic contribution—as photoexcited electrons decay by releasing energy into the lattice—and of an oscillating signal due to DECP.

For Bi and Sb, we analyze the data according to the DECP model developed in Ref. 15. We describe the signal rise with an error function, the electronic response with an exponential decay, and the coherent phonon with a damped oscillation. The resulting fit function reads

$$\frac{\Delta R(t)}{R} = \frac{1}{2} \left[1 + \text{erf} \left(\frac{t - t_0}{\tau_0} \right) \right] \\
\times \left\{ A_0 + A_1 e^{-(t - t_0/\tau_1)} + A_{\text{osc}} e^{-(t - t_0/\tau_{\text{osc}})} \\
\times \cos[\omega_{\text{osc}}(t - t_0) + \phi_{\text{osc}}] \right\}, \tag{9}$$

Table I. Coherent phonon parameters from fits to the time-dependent differential reflectivity $[\Delta R/R](t)$ for an incident pump fluence of $65\pm 1 \,\mu$ J/cm².

Material	$\omega_{ m osc}/2\pi({ m THz})$	Γ(THz)	$A_{ m osc}\cdot 10^{-5}$
Bi	2.8874 ± 0.0092	0.165 ± 0.018	10.05 ± 0.83
Sb	4.4886 ± 0.0090	0.186 ± 0.018	3.00 ± 0.21
$1T$ -TaS $_2$	1.658 ± 0.019	1.93 ± 0.12	48.9 ± 6.1

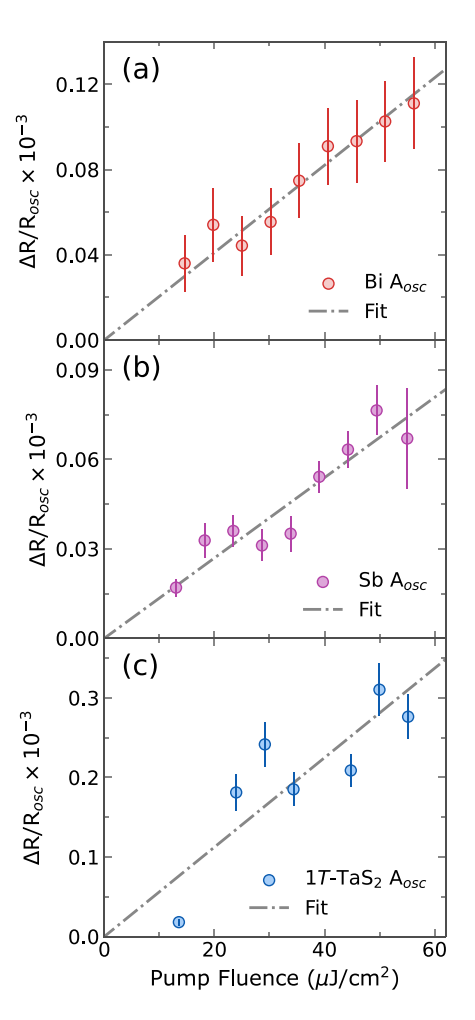


Fig. 5. Fluence dependence of the coherent phonon oscillation amplitude in (a) Bi, (b) Sb, and (c) 1T-TaS₂. Error bars represent uncertainties from the $\Delta R/R$ fits, while dashed-dotted grey lines are linear fits to the fluence-dependent data.

where t_0 is the time zero, τ_0 is the signal rise time, A_1 and τ_1 are the amplitude and lifetime of the electronic exponential, and A_0 is a long-lived electronic component. $A_{\rm osc}$, $\tau_{\rm osc}$, $\omega_{\rm osc}$, and $\phi_{\rm osc}$ are, respectively, the amplitude, decay time, angular frequency, and phase of the coherent phonon oscillation. For 1T-TaS $_2$, the constant component A_0 in Eq. (9) is replaced by a second exponential.

We additionally compute the Fourier transform of each of the oscillatory components after subtracting the fitted electronic contributions from the differential reflectivity. Each Fourier transform is then modeled by a Lorentzian with an added constant background to determine the frequency and

Table II. Ionic displacements and physical properties of Bi (Refs. 39 and 40), Sb (Refs. 41 and 42), and 1*T*-TaS₂ (Refs. 43 and 44). The displacements are calculated from the time-domain fit parameters.

Material	$U_0 \cdot 10^{-3} (\text{Å})$ at $\mathcal{F}(\text{mJ/cm}^2)$	$ ho$ (amu $/ ext{Å}^3$)	$ \epsilon $ at 1560 nm
Bi	0.850 at 0.035	5.907 (Refs. 39, 40, 45 and 46)	80.5 (Ref. 47)
Sb	0.874 at 0.039	4.031 (Refs. 41, 42, 45, and 46)	57.2 (Ref. 47)
1 <i>T</i> -TaS ₂	3.25 at 0.034	4.270 (Refs. 43–46)	30.0 (Refs. 48 and 49)

width of the observed oscillations. Fourier transforms for each sample are reported in Figs. 4(b)–4(f), while coherent phonon parameters from fits to the time-dependent reflectivity curves are reported in Table I. The obtained phonon frequencies are in excellent agreement with existing literature for Bi, ¹⁴, ¹⁵, ³⁰, ³¹ Sb, ¹⁴, ¹⁵, ³⁰ and 1*T*-TaS₂. ^{32–34} We note that phonons in Bi and Sb are more damped than those in Ref. 15 and quantitatively in agreement with the high-fluence damping reported in Ref. 31. This is likely due to thermal effects introduced by the 100-mW average power of the pump. Such an effect is not detected in 1T-TaS₂, likely due to its larger damping at equilibrium. ³³

A comparison of frequency and damping across the three materials allows us to establish connections between the observed oscillations and the microscopic physics of these ionic motions. By comparing the oscillation frequencies of Bi and Sb, we can directly verify the dependence of phonon frequency on the atomic mass $\omega_{osc}=\sqrt{k/\mu^*}.$ Both Bi and Sb crystals are semimetals crystallizing in the same rhombohedral unit cell, containing two atoms³⁵ and with nearest neighbor bond lengths differing by only 5%. This similarity suggests a close value of their elastic constants k. The reduced atomic masses μ^* of the two elements are instead quite different and equal to 104.49 amu (Bi) and 60.75 amu (Sb). ³⁶ The coherent phonon frequency ratio $\omega_{osc}^{Sb}/\omega_{osc}^{Bi} \sim$ 1.55 is very close to that expected from their relative atomic masses $\sqrt{\mu_{\rm Bi}^*/\mu_{\rm Sb}^*}\sim$ 1.31, thus providing a vivid demonstration that lighter nuclei oscillate faster than heavier ones.

Further microscopic insight can be gained by comparing the damping of these oscillations. Coherent phonons in Bi and Sb are long-lived, while those in 1T-TaS₂ are an order of magnitude more damped and observable over just two cycles. Phonons in metals and semimetals can decay into low-energy electron-hole pairs or into other phonons via anharmonic coupling. Their damping rate Γ is proportional to the microscopic electron-phonon coupling constant of a material³⁷ and, hence, directly determined by the microscopic interactions with its surrounding environment. The 1T-TaS₂ phonon is associated with a structural distortion accompanying an electronic transition of this material into a charge-ordered phase.³³ This implies that its electron– phonon coupling is much larger than the ones of the other two systems, ³⁸ and together with the availability of photogenerated particle-hole pairs, this coupling produces an enhanced damping of the coherent oscillations in the time-domain.

C. Fluence dependence

We also measure the behavior of the coherent phonons as functions of the incident pump fluence. Intuitively, a larger laser fluence will induce a larger number of electronic transitions and a larger redistribution of electronic density. 15 We test this expectation by systematically attenuating the pump power at the sample with a waveplate and a polarizer. The pump fluence is calculated for a 31- μ m pump diameter at the sample. Upon varying the incident pump fluence in all three samples, we do not observe significant changes of phonon frequencies or dampings. However, we do observe a linear dependence of the signal amplitude in both electronic and coherent phonon contributions, as shown in Fig. 5. This observation agrees with previous reports in the literature, 31,34 and is consistent with a linear increase in electronic transitions due to the pump absorption. 15 By fitting a line to the coherent phonon amplitude $\Delta R/R_{\rm osc}$ as function of fluence \mathcal{F} , we extract

slopes of $(2.051 \pm 0.062) \cdot 10^{-3}$, $(1.346 \pm 0.066) \cdot 10^{-3}$, and $(5.62 \pm 0.50) \cdot 10^{-3}$ cm²/mJ for Bi, Sb, and 1*T*-TaS₂, respectively.

We finally estimate the ionic displacements introduced by the pump. We link the ionic displacement U_0 to the pump fluence \mathcal{F} and the coherent phonon amplitude $\Delta R/R_{\rm osc}$ by rewriting Eq. (8) in practical units,³¹

$$U_0 = \sqrt{\left(\frac{\Delta R}{R}\right)_{\mathcal{F}} \frac{377 \times \mathcal{F}}{\rho \nu_0 |\epsilon|}},\tag{10}$$

where \mathcal{F} is given in mJ/cm², ρ is the sample density in amu/ų, ν_0 is the frequency of incident light in THz, and $\epsilon = \sqrt{\epsilon_1^2 + \epsilon_2^2}$ is the modulus of the complex dielectric constant of the sample. The ionic displacements and relevant dielectric constants used for calculation are additionally reported in Tables II and are compatible with those reported in Ref. 31.

V. CONCLUSIONS

In summary, we have developed an ultrafast coherent phonon spectroscopy experiment for the undergraduate instructional laboratory. By choosing a commercial and costeffective Er-fiber oscillator emitting light at 1560 nm with 50-fs pulse duration and 100-MHz repetition rate, we have lowered the barrier for the introduction of ultrafast optical spectroscopy in the undergraduate curriculum. Our experiment guides students through the basics of ultrafast laser pulse characterization and of coherent phonon spectroscopy in Bi, Sb, and 1T-TaS₂ samples. By connecting the measured ultrafast reflectivity changes with microscopic properties of the crystal lattice, we demonstrate the effectiveness of ultrafast optical spectroscopy as a fundamental probe of solids. With this relatively simple table-top experiment, students are able to directly observe ionic motions via macroscopic observables and tangibly appreciate concepts of introductory solid state physics. This experiment has been designed for a semester-long course of advanced laboratory (Physics 191 at Harvard University) in which students are required to complete three independent experiments ranging from optics to nuclear and condensed matter physics. Each experiment lasts 32 h distributed over eight four-hour sessions. However, its versatility and modular nature make it an ideal template for future advanced laboratories of varying timelines and curricular depth. Finally, the replacement of selected components could further drive down the setup costs and facilitate its diffusion in other undergraduate programs.

SUPPLEMENTARY MATERIAL

Please click on this link to access the supplementary material, which includes details about measurement and analysis of the differential reflectivity, as well as fluence-dependent data for the three compounds studied in this work. Print readers can see the supplementary material at https://doi.org/10.60893/figshare.ajp.c.7261363.

ACKNOWLEDGMENTS

The authors thank M. Först, J. Freericks, G. Kestin, A. Kogar, and R. Merlin for insightful discussions. The authors also thank C. Stubbs and L. McCarty, as well as the Harvard Faculty of Arts and Sciences, for supporting this project. M.M. gratefully acknowledges support by the NSF Award

No. DMR-2132338. The authors thank N. Tombros (HQ Graphene) for providing 1T-TaS $_2$ samples for a nominal fee and S. Teitelbaum for providing eigenvectors of the A_{1g} phonon mode of Bi in Fig. 1.

AUTHOR DECLARATIONS Conflict of Interest

The authors have no conflicts to disclose.

Table III. List of components of the ultrafast spectroscopy experiment with reduced-cost alternatives in brackets. Bracketed items are suited to replace all other components within the relevant subsection. The total includes the cost of the listed instrumentation, while the option total assumes the substitution of the preceding items in each table cell with the bracketed alternative.

Manufacturer	Model number	Item	Price (\$)
Laser			
Menlo systems	ELMO/ELMA	Femtosecond oscillator and amplifier	32 000
(lab-made)		Mode-locked fiber laser	7400^{26}
Laservision	F42.P1M01.5000	Laser safety glasses (×4)	720
Thorlabs	PM100D	Power meter	1250
Thorlabs	S144C	IR detector for power meter	950
Thorlabs	VRC4	IR card	90
Thorlabs	B3060G	$30'' \times 60'' \times 4''$ optical breadboard	2290
Thorlabs	MC2000B	Optical chopper and blades	1600
Lock-in amplifier			
Stanford Research	SR830	Autophasing lock-in amplifier	5400
(Stanford Research)	(SR510)	Lock-in amplifier	3000
Delay stage components		•	
Newport	436	Translation stage	710
Newport	LTA-HS	Actuator	1970
Newport	SMC100CC	Controller	1150
Newport	SMC-USB	USB interface	110
Newport	SMC-PS80	Power supply	160
(Thorlabs)	(PT1-Z8)	DC motorized translation stage and accessories	1880
Sample stage components	(111 20)	De motorized transmitor stage and accessories	1000
Newport Stage components	426	Translation stage (\times 3)	1670
Newport	SM-25	Manual actuators (\times 3)	410
Newport	360-90	90° angle bracket	90
(Thorlabs)	(XR25P-K2)	3D translation stage	1650
Optics	(AR231 - R2)	3D translation stage	1030
Lattice electro optics	FABS-1560-Rp90-45-UF-1012	90/10 beamsplitter	810
Crylight photonics	BBO-5 × 5-0.1-19.8-P/P-D25.4	BBO crystal	330
Edmund optics	85–046	Half wave plate $(\times 2)$	740
*	34–314	• • • • • • • • • • • • • • • • • • • •	2760
Edmund optics Thorlabs	KS1RS	Wire grid polarizer (×3)	2700
Thorlabs		Rotation/tip/tilt mount for BBO	170
	RSP05	Rotation mount for polarization optics (\times 2)	
Thorlabs	HR1015-M01	Retroreflectors (×2)	480
Thorlabs	F220APC-1550	Fiber coupler	220
Thorlabs	LB2	Beam block	180
Thorlabs	LA5763	50-mm CaF ₂ lens	200
Thorlabs	LA5010	100-mm CaF ₂ lenses (×4)	480
Thorlabs	DET50B2	Photodiode for 1560 nm	480
Thorlabs	DET100A2	Photodiode for 780 nm	180
Thorlabs	CS165MU	Monochrome CMOS camera	470
Thorlabs	PF10-03-M01	Gold mirrors $(\times 5)$	280
Thorlabs	KM100	Mirror mounts ($\times 10$)	420
Thorlabs	PFD10-03-M01	Gold D mirror	70
Thorlabs	KM100DL	Left-handed D mirror mount	90
Thorlabs	ID8	Iris $(\times 8)$	460
Thorlabs	P300K, P100K, P50K	Pinholes $(\times 3)$	230
Thorlabs	SMR1	Mounts for pinholes $(\times 3)$	60
Thorlabs	TR3	Posts ($\times 30$)	170
Thorlabs	PH3	Post holder (\times 30)	280
Thorlabs	BE1	Base (×30)	330
Thorlabs	CF125	Clamping fork (\times 30)	280
			Total: \$61 010
			(Option total: \$31 270)

APPENDIX: COST BREAKDOWN

We report the cost of the components used in our pumpprobe setup as well as reduced-cost options in Table III. Several components such as the autophasing lock-in amplifier and a commercial fiber laser were selected over more cost-efficient alternatives out of convenience. An amended price guide with reasonable alternatives brings the total cost down to approximately \$31000.

- ^{a)}ORCID: 0000-0003-4877-7997.
- b)ORCID: 0009-0004-9894-1294.
- c)ORCID: 0000-0001-7515-0626.
- ^{d)}ORCID: 0009-0003-8890-023X.
- e)ORCID: 0000-0002-3961-8524.
- f)Electronic mail: mmitrano@g.harvard.edu, ORCID: 0000-0002-0102-
- ¹R. D. Averitt and A. J. Taylor, "Ultrafast optical and far-infrared quasiparticle dynamics in correlated electron materials," J. Phys.: Condens. Matter **14**(50), R1357–R1390 (2002).
- ²A. Kirilyuk, A. V. Kimel, and T. Rasing, "Ultrafast optical manipulation of magnetic order," Rev. Mod. Phys. 82(3), 2731–2784 (2010).
- ³D. Basov, R. Averitt, D. van der Marel, M. Dressel, and K. Haule, "Electrodynamics of correlated electron materials," Rev. Mod. Phys. **83**(2), 471–541 (2011).
- ⁴J. Orenstein, "Ultrafast spectroscopy of quantum materials," Phys. Today **65**(9), 44–50 (2012).
- ⁵J. Zhang and R. Averitt, "Dynamics and control in complex transition metal oxides," Annu. Rev. Mater. Res. 44(1), 19–43 (2014).
- ⁶C. Giannetti, M. Capone, D. Fausti, M. Fabrizio, F. Parmigiani, and D. Mihailovic, "Ultrafast optical spectroscopy of strongly correlated materials and high-temperature superconductors: A non-equilibrium approach," Adv. Phys. **65**(2), 58–238 (2016).
- ⁷A. de la Torre, D. M. Kennes, M. Claassen, S. Gerber, J. W. McIver, and M. A. Sentef, "Colloquium: Nonthermal pathways to ultrafast control in quantum materials," Rev. Mod. Phys. **93**(4), 041002 (2021).
- ⁸D. Basov, R. Averitt, and D. Hsieh, "Towards properties on demand in quantum materials," Nat. Mater. **16**(11), 1077–1088 (2017).
- ⁹T. D. Donnelly and C. Grossman, "Ultrafast phenomena: A laboratory experiment for undergraduates," Am. J. Phys. 66(8), 677–685 (1998).
- ¹⁰M. Sullivan, S. Desmarais, E. Pacheco, M. Hamalian, E. Moutsopoulos, H. Patel, S. Scala, Y. Sudhu, and C. Schnitzer, "Femtosecond laser spectroscopy, autocorrelation, and second harmonic generation: An experiment for undergraduate students," Eur. J. Phys. 40(3), 035302 (2019).
- ¹¹J. Donnelly and F. E. Hernandez, "Two-photon absorption spectroscopy on curcumin in solution: A state-of-the-art physical chemistry experiment," J. Chem. Educ. 94(1), 101–104 (2017).
- ¹²I. J. Porter, M. W. Zuerch, A. M. Baranger, and S. R. Leone, "Coherent phonons in antimony: An undergraduate physical chemistry solid-state ultrafast laser spectroscopy experiment," J. Chem. Educ. 100(1), 342–349 (2023).
- ¹³S. De Silvestri, J. Fujimoto, E. Ippen, E. B. Gamble, L. R. Williams, and K. A. Nelson, "Femtosecond time-resolved measurements of optic phonon dephasing by impulsive stimulated Raman scattering in α-perylene crystal from 20 to 300 K," Chem. Phys. Lett. **116**(2–3), 146–152 (1985).
- ¹⁴T.-K. Cheng, J. Vidal, H. J. Zeiger, G. F. Dresselhaus, M. S. Dresselhaus, and E. P. Ippen, "Mechanism for displacive excitation of coherent phonons in Sb, Bi, Te, and Ti₂O₃," Appl. Phys. Lett. **59**(16), 1923–1925 (1991).
- ¹⁵H. J. Zeiger, J. Vidal, T. K. Cheng, E. P. Ippen, G. Dresselhaus, and M. S. Dresselhaus, "Theory for displacive excitation of coherent phonons," Phys. Rev. B 45(2), 768–778 (1992).
- ¹⁶N. Ashcroft and N. Mermin, *Solid State Physics* (Saunders College, Philadelphia, 1976).
- ¹⁷S. H. Simon, *The Oxford Solid State Basics* (Oxford U. P., Oxford, UK, 2013).
- ¹⁸R. Merlin, "Generating coherent THz phonons with light pulses," Solid State Commun. **102**(2–3), 207–220 (1997).
- ¹⁹T. Dekorsy, G. C. Cho, and H. Kurz, "Coherent phonons in condensed media," in *Light Scattering in Solids VIII: Fullerenes, Semiconductor Surfaces, Coherent Phonons*, edited by M. Cardona and G. Güntherodt (Springer Berlin Heidelberg, Berlin/Heidelberg, 2000), pp. 169–209.
- ²⁰T. E. Stevens, J. Kuhl, and R. Merlin, "Coherent phonon generation and the two stimulated Raman tensors," Phys. Rev. B 65(14), 144304 (2002).

- ²¹J. J. Li, J. Chen, D. A. Reis, S. Fahy, and R. Merlin, "Optical probing of ultrafast electronic decay in Bi and Sb with slow phonons," Phys. Rev. Lett. 110(4), 047401 (2013).
- ²²A. V. Kuznetsov and C. J. Stanton, "Theory of coherent phonon oscillations in semiconductors," Phys. Rev. Lett. 73(24), 3243–3246 (1994).
- ²³M. S. Dresselhaus, G. Dresselhaus, and A. Jorio, *Group Theory—Application to the Physics of Condensed Matter* (Springer-Verlag, Berlin Heidelberg, 2008).
- ²⁴A. Kogar, "Coherent phonons: Mechanisms, phases and symmetry," Condensed Life blog (2021), https://thiscondensedlife.wordpress.com/2021/10/09/coherent-phonons-mechanisms-phases-and-symmetry/.
- ²⁵M. F. DeCamp, "Seeing sound: Dynamical effects in ultrafast x-ray diffraction," Ph.D. thesis (University of Michigan, Horace H. Rackham School of Graduate Studies, 2002).
- ²⁶D. Upcraft, A. Schaffer, C. Fredrick, D. Mohr, N. Parks, A. Thomas, E. Sievert, A. Riedemann, C. W. Hoyt, and R. J. Jones, "Ultrafast optics with a mode-locked erbium fiber laser in the undergraduate laboratory," Am. J. Phys. 89(12), 1152–1160 (2021).
- ²⁷A. Weiner, *Ultrafast Optics* (John Wiley & Sons, Inc., Hoboken, NJ, 2009), pp. 1–580.
- ²⁸E. P. Ippen and C. V. Shank, "Techniques for measurement," in *Ultrashort Light Pulses: Picosecond Techniques and Applications*, edited by S. L. Shapiro (Springer Berlin Heidelberg, Berlin, Heidelberg, 1977), pp. 83–122
- ²⁹Menlo Systems GmbH, Private Communication (December, 2022).
- ³⁰J. S. Lannin, J. M. Calleja, and M. Cardona, "Second-order Raman scattering in the group-Vb semimetals: Bi, Sb, and As," Phys. Rev. B 12(2), 585–593 (1975).
- ³¹M. F. DeCamp, D. A. Reis, P. H. Bucksbaum, and R. Merlin, "Dynamics and coherent control of high-amplitude optical phonons in bismuth," Phys. Rev. B 64(9), 092301 (2001).
- ³²S. Sugai, "Lattice vibrations in the charge-density-wave states of layered transition metal dichalcogenides," Phys. Status Solidi B 129(1), 13–39 (1985).
- ³³J. Demsar, L. Forró, H. Berger, and D. Mihailovic, "Femtosecond snapshots of gap-forming charge-density-wave correlations in quasi-twodimensional dichalcogenides 1T-TaS₂ and 2H-TaSe₂," Phys. Rev. B 66(4), 041101 (2002).
- ³⁴A. Mann, E. Baldini, A. Odeh, A. Magrez, H. Berger, and F. Carbone, "Probing the coupling between a doublon excitation and the charge-density wave in TaS₂ by ultrafast optical spectroscopy," Phys. Rev. B **94**(11), 115122 (2016)
- ³⁵X. Gonze, J.-P. Michenaud, and J.-P. Vigneron, "First-principles study of As, Sb, and Bi electronic properties," Phys. Rev. B 41(17), 11827–11836 (1990).
- ³⁶CRC Handbook, CRC Handbook of Chemistry and Physics, 88th ed. (Taylor and Francis, Boca Raton, FL, 2007).
- ³⁷P. B. Allen, "Neutron spectroscopy of superconductors," Phys. Rev. B **6**(7), 2577–2579 (1972).
- ³⁸L. Perfetti, P. A. Loukakos, M. Lisowski, U. Bovensiepen, H. Berger, S. Biermann, P. S. Cornaglia, A. Georges, and M. Wolf, "Time evolution of the electronic structure of 1T-TaS₂ through the insulator-metal transition," Phys. Rev. Lett. 97(6), 067402 (2006).
- ³⁹"Bismuth (Bi) lattice and structural parameters, thermal expansion, atomic weight and volume," in *Semiconductors: Non-Tetrahedrally Bonded Elements and Binary Compounds I*, Landolt-Börnstein—Group III Condensed Matter Vol. 41C, edited by O. Madelung, U. Rössler, and M. Schulz (Springer-Verlag, Berlin, Heidelberg, 1998).
- 40. Bismuth (Bi) crystal structure, chemical bond," Non-Tetrahedrally Bonded Elements and Binary Compounds I, Landolt-Börnstein—Group III Condensed Matter Vol. 41C, edited by O. Madelung, U. Rössler, and M. Schulz (Springer-Verlag, Berlin, Heidelberg, 1998).
- 41"Antimony (Sb) lattice and structural parameters, thermal expansion," Non-Tetrahedrally Bonded Elements and Binary Compounds I, Landolt-Börnstein—Group III Condensed Matter Vol. 41C, edited by O. Madelung, U. Rössler, and M. Schulz (Springer-Verlag, Berlin, Heidelberg, 1998).
- ⁴²"Antimony (Sb) structure, chemical bond," *Non-Tetrahedrally Bonded Elements and Binary Compounds I*, Landolt-Börnstein—Group III Condensed Matter Vol. 41C, edited by O. Madelung, U. Rössler, and M. Schulz (Springer-Verlag, Berlin, Heidelberg, 1998).
- ⁴³"TaS₂: Crystal structure, physical properties," *Non-Tetrahedrally Bonded Elements and Binary Compounds II*, Landolt-Börnstein—Group III Condensed Matter Vol. 41D, edited by O. Madelung, U. Rössler, and M. Schulz (Springer-Verlag, Berlin, Heidelberg, 2000).
- ⁴⁴G. Hagg and N. Schonberg, "X-ray studies of sulfides of titanium, zirconium, niobium, and tantalum," Ark. Kemi 7, 371–380 (1954).

45. Standard atomic weights," CRC Handbook of Chemistry and Physics, Internet Version, 87th ed., edited by D. R. Lide, G. Baysinger, L. I. Berger, R. N. Goldberg, H. V. Kehiaian, K. Kuchitsu, D. L. Roth, and D. Zwillinger (Taylor and Francis, Boca Raton, FL, 2007).

⁴⁶Y. Liao, Practical Electron Microscopy and Database (2006), Chap. Table 3033. Volume of unit cells in crystal structures, https://www.globalsino.com/EM/.

- ⁴⁷A. P. Lenham, D. M. Treherne, and R. J. Metcalfe, "Optical properties of antimony and bismuth crystals," J. Opt. Soc. Am. 55(9), 1072 (1965).
- ⁴⁸N. Dean, "Electronic and structural dynamics of complex materials," Ph.D. thesis (University of Oxford, 2010).
- ⁴⁹ A. R. Beal, H. P. Hughes, and W. Y. Liang, "The reflectivity spectra of some group VA transition metal dichalcogenides," J. Phys. C 8(24), 4236–4234 (1975).



NOT THAT I DON'T DESERVE IT.
THESE TWO NOBELS AIN'T DECORATIVE.
BUT I MAKE A SORRY ROLE MODEL IF
GIRLS JUST SEE ME OVER AND OVER
AS THE ONE TOKEN (ADY SCIENTIST.



LISE MEITNER FIGURED OUT THAT NUCLEAR FISSION WAS HAPPENING, WHILE HER COLLEAGUE OTTO WAS STARING BLANKLY AT THEIR DATA IN CONFUSION, AND PROVED ENRICO FERMI WRONG IN THE PROCESS. ENRICO AND OTTO BOTH GOT NOBEL PRIZES. LISE GOT A NATIONAL WOMEN'S PRESS CLUB AWARD.



THEY FINALLY NAMED AN ELEMENT AFTER HER, BUT NOTUNTIL 60 YEARS LATER.

EMMY NOETHER FOUGHT PAST HER VICTORIAN-ERA FINISHING-SCHOOL UPBRINGING PURSUED MATHEMATICS BY AUDITING CLASSES, AND, AFTER FINALLY GETTING A PH.D, WAS PERMITTED TO TEACH ONLY AS AN UNPAID LECTURER (OFTEN UNDER MALE COLLEAGUES' NAMES).

WAS SHE AS GOOD AS THEM?



SHE REVOLUTIONIZED ABSTRACT ALGEBRA, FILLED GAPS IN RELATIVITY, AND FOUND WHAT SOME CALL THE MOST BEAUTIFUL, DEEPEST RESULT IN THEORETICAL PHYSICS.

BUT YOU DON'T BECOME GREAT BY TRYING TO BE GREAT. YOU BECOME GREAT BY WANTING TO DO SOMETHING, AND THEN DOING IT SO HARD THAT YOU BECOME GREAT IN THE PROCESS.



(Source: https://xkcd.com/896)

SO DON'T TRY TO BE THE NEXT ME, NOETHER, OR MEITNER. JUST REMEMBER THAT IF YOU WANT TO DO THIS STUFF, YOU'RE NOT ALONE.

